Exp Fluids (2008) 44:973–984
DOI 10.1007/s00348-007-0456-2

RESEARCH ARTICLE

Experimental study of heat flux in mixed convective flow over solid waves

Simon Kuhn · Philipp Rudolf von Rohr

Received: 6 July 2007 / Revised: 7 December 2007 / Accepted: 14 December 2007 / Published online: 9 January 2008

Abstract In this experimental study, we address transport processes in a mixed convective flow over a heated wavy surface. Therefore, we combine digital particle image velocimetry (DPIV) and two-color planar laser induced fluorescence (PLIF) to simultaneously measure the velocity and temperature field. For this, we propose to use the dye combination Rhodamine B and Rhodamine 110, both excited with the Nd:YAG laser also used for the PIV measurements. We investigate the influence of mixed convection over a wavy surface on the velocity field, turbulence statistics, the temperature field and the heat flux. By computing these quantities we find a correlation between the maximum in the Reynolds stress profiles and the components of the heat flux vector, thus regions of maximum momentum and scalar transport coincide. In addition, we apply a proper orthogonal decomposition (POD) to extract the most dominant flow structures in a measurement plane above the wavy surface. This first POD mode is identified as streamwise-oriented, counter-rotating vortices whose spanwise scaling is also correlated with the maximum of heat flux.

List of symbols

a	half-amplitude of the wave profile
B	channel width
g	acceleration due to gravity
Gr_H	Grashof number
H	full channel height
$\dot{q}$	heat flux
Re_H	Reynolds number
t	time
T	temperature
u,v,w	components of the instantaneous fluid velocity
U_B	bulk velocity (channel flow)
x,y,z	Cartesian coordinates
$\mathbf{X}$	spatiotemporal set of data
y_w	profile of the wavy bottom wall

Greek symbols

α	amplitude-to-wavelength ratio, $2a/\Lambda$
β	volumetric thermal expansion coefficient
λ_i	eigenvalue of POD mode i
Λ	wavelength of the sinusoidal profile at the bottom wall
ν	kinematic viscosity
Π_i	eigenfunction of POD mode i

Abbreviations

CCD	charge coupled device
DPIV	digital particle image velocimetry
FOV	field of view
Nd:YAG	neodymium:yttrium aluminium garnet ($Y_3Al_5O_{12}$) crystal
PLIF	planar laser-induced fluorescence
PVC	poly vinyl chloride

Subscript

B	bulk quantity
H	channel height (used as length scale)

S. Kuhn · P. Rudolf von Rohr (✉)
Institute of Process Engineering,
ETH Zurich Sonneggstrasse 3,
8092 Zurich, Switzerland
e-mail: vonrohr@ipe.mavt.ethz.ch

S. Kuhn
e-mail: kuhn@ipe.mavt.ethz.ch

1 Introduction

Flows in the mixed convective regime are present in relevant technical and geophysical flow situations. Especially in technical applications, the flow boundaries resemble complex wall geometries, e.g. undulations in heat exchangers to enhance transport processes (e.g. Rush et al. 1999; Dellil et al. 2004). Previous studies of mixed convective flows focused mainly on horizontal parallel plate configurations. Osborne and Incropera (1985a, b) and Maughan and Incropera (1989) investigated laminar, transitional, and turbulent mixed convection heat transfer for a horizontal parallel plate water channel experimentally. They found an increase in heat transfer due to buoyancy effects which is less pronounced for higher Reynolds numbers and is preceded by the onset of a secondary flow. The structure of this secondary flow in a mixed convective air flow through a horizontal plane channel was investigated numerically and experimentally by Yu et al. (1997a, b). Their results showed that this secondary flow is in the form of longitudinal vortex rolls for high enough Reynolds numbers. To enhance the complexity of the investigated flow situation wavy walls are often chosen as a well-defined bounding surface of the flow. Several numerical studies addressed convective heat transfer in channel flow bound by one or two wavy walls (e.g. Dellil et al. 2004; Metwally and Manglik 2004). In a recent experimental study, Kruse and Rudolf von Rohr (2006) investigated the transport of heat (as a passive scalar) in a turbulent flow over a heated wavy wall. By employing a particle image thermometry technique the velocity and temperature fields were measured simultaneously. Quantitative agreement between large-scale thermal and momentum structures was found. The present work advances this study by addressing buoyancy effects induced by mixed convection from a wavy surface on transport processes by applying a combined digital particle image velocimetry and laser-induced fluorescence technique to simultaneously measure the velocity and the temperature field.

Non-invasive measurement techniques to assess the temperature field in a fluid are another important topic in recent research. One common technique is based on liquid crystals (Dabiri and Gharib 1991) which is known as particle image thermometry and can also be used together with PIV to obtain simultaneous measurements (Kruse and Rudolf von Rohr 2006). To assess the temperature field thermochromic liquid crystals dispersed in the fluid are illuminated with a sheet of white light. The color distribution reflected by the particles is recorded by a color CCD. In a first step the red, green, and blue intensities of the color distribution are converted into a local intensity, local hue, and saturation, this process is also known as RGB to HSI conversion. The temperature information is obtained by providing a calibration function between the local fluid temperature and the local hue. Major drawbacks of this technique are the need for a color CCD to record the color information emitted from the liquid crystals and, if simultaneous measurements are desired, the use of two different light sources which makes it complicate to synchronize the whole measurement system. Another whole-field technique is based on laser-induced fluorescence where temperature sensitive fluorescent dyes excitable by laser light are employed. As light sources, both constant wavelength Ar^+ ion lasers and pulsed Nd:YAG lasers are possible. However, to examine larger regions in the flow field and to acquire instantaneous images the use of pulsed Nd:YAG lasers is preferable (Karasso and Mungal 1997). Coolen et al. (1999) report on one-color LIF temperature measurements with Rhodamine B as temperature sensitive dye excited with a Nd:YAG laser. The variation of the exciting light intensity, caused by different reasons such as optics or even refraction of the light passing through the thermal field itself, is a source of measurement inaccuracy. Thus, Sakakibara and Adrian (1999, 2004) proposed the use of two-color LIF where one fluorescent dye is temperature sensitive, the other insensitive and used as correction for inhomogeneities in the laser light sheet. The ratio of the emitted light of both dyes is then calibrated and used to calculate the temperature in the flow field. By applying this method of two-color LIF the concentration ratio of the two dyes has to be known and kept constant during measurement, which might pose a difficulty for example in turbulent diffusion processes. To address this problem the two-color/single-dye technique was introduced. Bruchhausen et al. (2005) report on two-color LIF with the use of two spectral bands of Rhodamine B as single fluorescent dye. Therefore, these spectral bands need to exhibit a strong difference in their temperature sensitivity. By applying this technique, the ratio of the emitted fluorescence signal depends solely on the temperature of the fluid.

This experimental study addresses the mixed convective flow between a flat top wall and a heated wavy bottom wall. Thus transport processes in a complex flow situation, characterized by buoyancy effects, separation and reattachment of the flow due to the presence of the wavy wall, are evaluated. We present simultaneous measurements of the two-dimensional fluid velocity and temperature fields by using a combined digital particle image velocimetry (DPIV) and two-color planar laser-induced fluorescence (PLIF) technique.

2 Flow description

We investigate the mixed convective channel flow between a heated sinusoidal bottom surface and a flat top wall. This

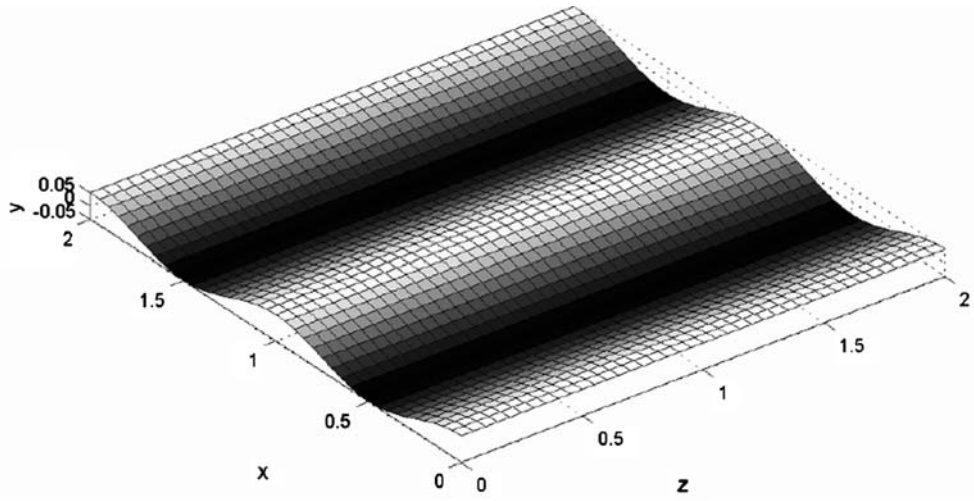

Fig. 1 Profile of the wavy wall characterized by $\alpha = 0.1$ and $\Lambda = 30$ mm

sinusoidal bottom surface is characterized by the amplitude-to-wavelength ratio of $\alpha = 2a/\Lambda = 0.1$, its wavelength is $\Lambda = 30$ mm, which is equal to the total channel height H. The profile of the wavy wall $y_w(x)$ is depicted in Fig. 1, which is mathematically described as

$$y_w(x) = a \sin\left(\frac{2\pi x}{\Lambda}\right). \quad (1)$$

Figure 1 also shows the used coordinate system: x denotes the streamwise coordinate direction, y the vertical and z the spanwise direction. The corresponding velocity components are denoted as u, v, and w.

The mixed convective flow is characterized by the Reynolds number and the Grashof number. The Reynolds number Re_H is calculated according to

$$Re_H = \frac{U_B H}{\nu}, \quad (2)$$

where ν denotes the kinematic viscosity, H is the total height of the channel, and the bulk velocity U_B is given by

$$U_B = \frac{1}{H - y_w} \int_{y_w}^{H} U(x_\xi, y) \mathrm{d}y, \quad (3)$$

where x_ξ denotes an arbitrary x-location, and y_w describes the wave profile. The Grashof number Gr_H is given by

$$Gr_H = \frac{gH^3 \Delta T \beta}{\nu^2}, \quad (4)$$

where ΔT denotes the temperature difference between the bottom and top wall, and β is the volumetric thermal expansion coefficient. The ratio between the Grashof and the Reynolds number squared (Gr_H/Re_H^2) characterizes the convective regime of the flow. This ratio is in the range of unity for mixed convection, much smaller than one for forced convection, and much greater than one for natural convection (Incropera and DeWitt 2002).

The isothermal flow over a train of solid waves is connected to a developing shear layer, formed by the separation of the flow shortly after the wave crest, which extends over the whole wavelength. Figure 2 schematically illustrates characteristic regions of the flow field in the vicinity of the wavy surface reported by Cherukat et al. (1998), and Henn and Sykes (1999). These characteristic regions are the separation region (I), and the regions of maximum positive (II) and maximum negative (III) Reynolds shear stress $-\varrho\overline{u'v'}$. For smooth walls flow-oriented vortical eddies have been associated with large Reynolds stresses, and with the production of turbulence in the viscous region close to the wall (Brooke and Hanratty 1993). In earlier studies, Günther and Rudolf von Rohr (2003), Kruse et al. (2003, 2006), Kuhn et al. (2007), and Wagner et al. (2007) investigated the structure and dynamics of turbulent motions in a developed turbulent flow over various wavy surfaces and identified flow-oriented large-scale structures which contribute most to the momentum transport.

The results reported here are for the mixed convective regime at a Reynolds number of $Re_H = 1{,}100$ and a Grashof number of $Gr_H = 1.94 \times 10^6$ ($Gr_H/Re_H^2 = 1.6$), and for reference purposes for the isothermal case at $Re_H = 1{,}025$. At these conditions, we obtained a temperature difference between the wavy wall and the top wall of 8.5°C, respectively 5.5°C, for the difference between the wavy wall temperature and the bulk fluid temperature.

3 Experiments

The experiments are performed in the flow channel facility depicted in Fig. 3, for a detailed description we refer to Günther and Rudolf von Rohr (2003). The working fluid is deionized and filtered water, the channel facility is made of

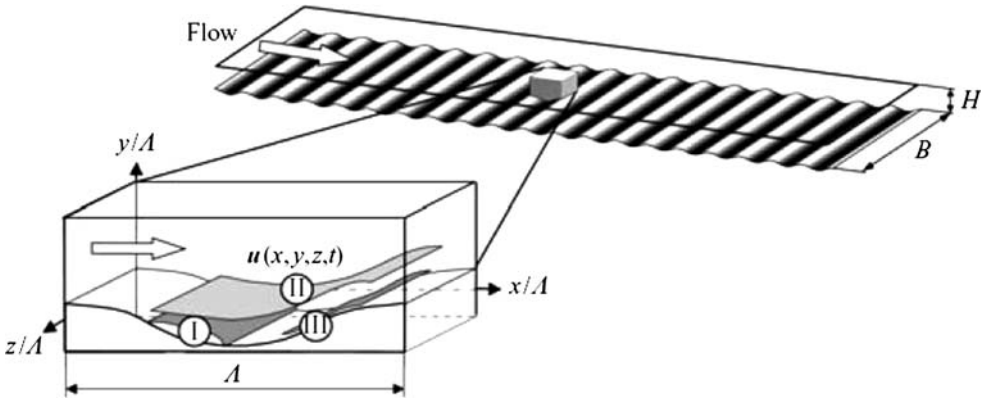

Fig. 2 Schematic of (I) the separation region, and the regions (II) of maximum positive and (III) maximum negative Reynolds shear stress for a flow situation with separation

anodized and regular aluminium, PVC, and Schott BK-7 glass. The full height of the channel, H, is 30 mm, and its aspect ratio (width B to height H) is 12:1. The wavy bottom wall in the test section is made of aluminum and is heated with an embedded electrical heat foil ($\dot{q} = 1,800\,\mathrm{W/m^2}$), the top wall is kept at a constant temperature of $T = 20°\mathrm{C}$. Two temperature sensors are integrated in the top and bottom wall to control and to record the temperature during the measurements at the measurement location. A heat exchanger is incorporated in the reservoir (9) to remove the heat from the fluid after passing the test section and to thereby ensure a constant entry temperature into the test section. We report on measurements performed in the (x,y)- and the (x,z)-plane for a hydrodynamically developed flow after the 50th wave crest.

To assess the fluid velocity field, we employ two-component digital particle image velocimetry (DPIV) (Adrian 1991; Westerweel 1997; Raffel et al. 1998). The temperature field is measured by means of two-color planar laser induced fluorescence (PLIF) (Sakakibara and Adrian 1999, 2004). To address the scalar fluxes both measurement techniques are combined to simultaneously assess the velocity and the scalar fields. Therefore the cameras, the laser and the image acquisition software were synchronized by means of an adjustable timing unit (PIV Synchronizer, ILA GmbH). We consider an ensemble of 1,000 consecutive image pairs acquired at a frame rate of 4 Hz. The measurement system consisting of the laser, the laser optics, and the cameras, is positioned on a traverse that allows vertical adjustment with an accuracy of approximately 10 μm. A flashlamp-pumped dual Nd:YAG-laser (NewWave, 120 mJ) provides the pulse light source for both DPIV and PLIF.

For the DPIV measurements the flow is seeded with hollow glass spheres with a mean diameter of 10 μm (density 1.03 g/cm^3). The scattered light is recorded with a 10-bit CCD camera with a pixel-resolution of 1,280 × 1,024 pixels^2, which is equipped with a band-pass filter (passing light at 532 nm ± nm). The post-processing of the DPIV data is comprised of an adaptive cross-correlation algorithm, local filtering and interpolating of the filtered vectors. The measurement accuracy of DPIV is influenced by the particle image diameter, the particle image density, the particle image displacement and the velocity gradient within the interrogation area. Thus, the total error can be subdivided into errors resulting from the image processing (interrogation scheme) and errors resulting from the image recording. Due to the considered interrogation algorithm the error level for the image processing is estimated to be below 10^{-2} pixels (Scarano and Riethmuller 2000; Scarano 2002). The error caused by the optical imaging is determined to be 0.01% (Kruse 2005). Thus the uncertainty of the DPIV measurements resulting from the experimental setup, image acquisition and image processing is estimated to be in the order of 1%.

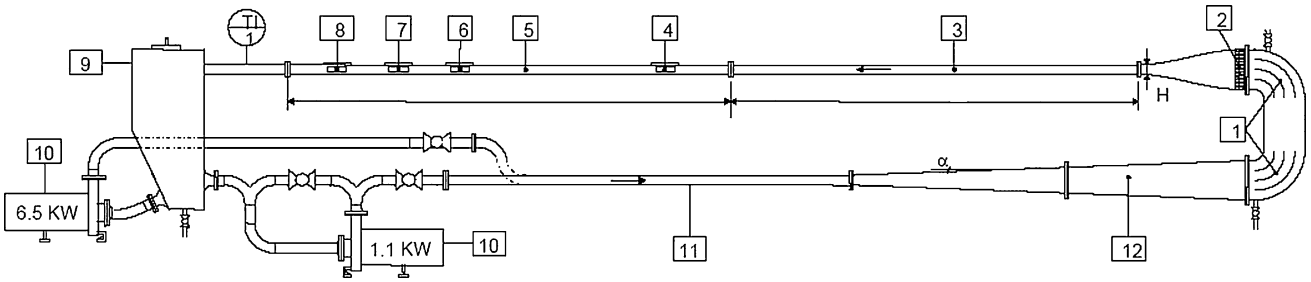

Fig. 3 Channel flow facility consisting of (*1*) turning elbows, (*2*) honeycomb, (*3*) flat-walled entrance section, (*5*) test section with wavy bottom and flat top wall, (*4*, *6–8*) optical viewports, (*9*) reservoir, (*10*) frequency controlled pumps, (*11*) pipe and (*12*) diffusor

In two-color PLIF, the intensity of emitted light of one dye is a function of the fluid temperature and is thus used to record the temperature information. The other dye is insensitive to temperature and is used to correct for inhomogeneities in the laser light sheet originating from the optics or from the thermal media itself. By calculating and calibrating the emitted light intensity ratios of both dyes the temperature field can be measured. For our measurements, we use Rhodamine B as temperature sensitive dye with a concentration of 125 µg/l, as temperature insensitive dye we choose Rhodamine 110 with a concentration of 150 µg/l. The fluorescent light is recorded with two 12-bit CCD cameras with a pixel-resolution of 1,376 × 1,040 pixels^2. A schematic of the optical setup is depicted in Fig. 4. To excite the dyes a Nd:YAG laser is used. Figures 5 and 6 depict the absorption spectra of Rhodamine B, respectively Rhodamine 110. These figures show that Rhodamine B exhibits good absorption at an exciting wavelength of 532 nm, whereas for Rhodamine 110 the exciting wavelength is situated at the tail of the absorption peak. To test the suitability of this dye combination we measured the emission spectra of a mixture of Rhodamine B and Rhodamine 110 excited at a wavelength of 532 nm which is depicted in Fig. 7. It is observed that the emission peaks of both dyes are pronounced and clearly distinguishable. Thus, we conclude that this dye combination is suitable for temperature measurements with Nd:YAG lasers.

The spectral characteristic of the beamsplitter (Laseroptik GmbH) exhibits a high transmittance at 520 nm and a high reflectance at 575 nm. Thus the emitted light from Rhodamine B and Rhodamine 110 is separated between the two CCDs. Since the flow is seeded the Mie scattering from the particles has to be removed from the emitted light of Rhodamine 110. This is accomplished by the filter mounted

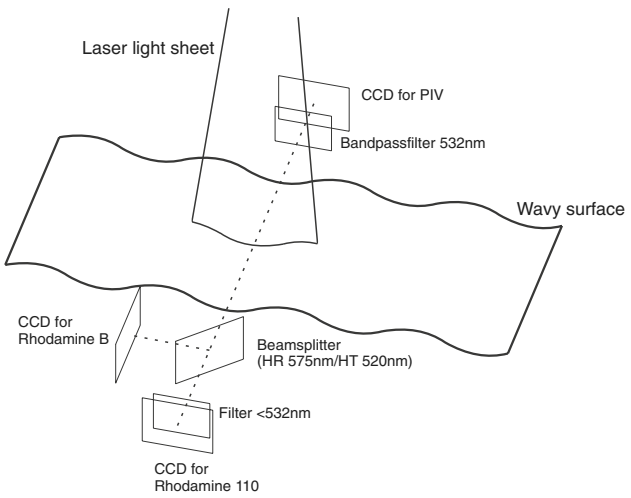

Fig. 4 Schematic of the optical setup (not to scale)

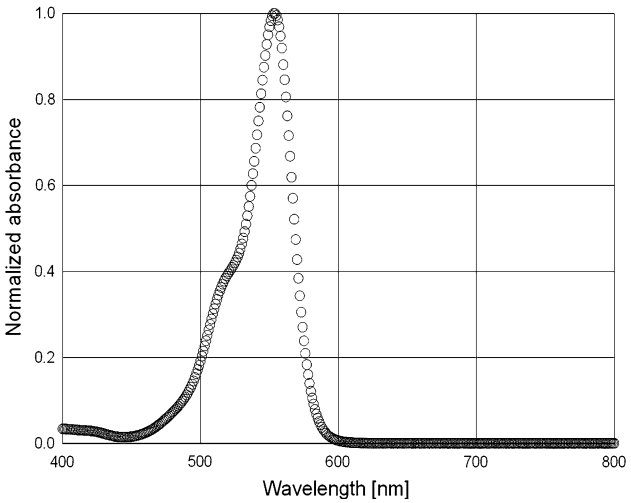

Fig. 5 Absorption spectrum of Rhodamine B

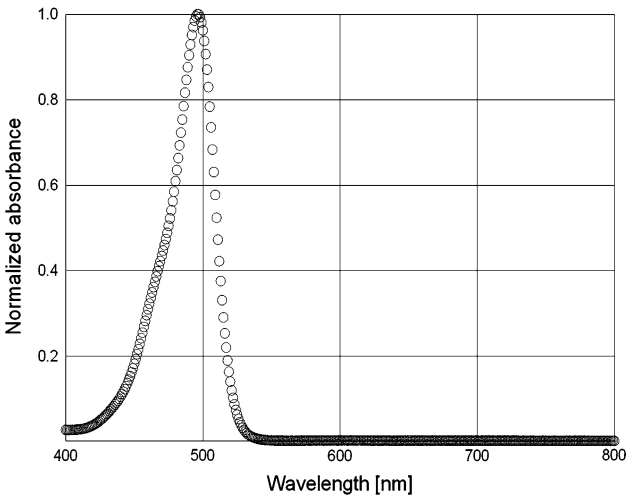

Fig. 6 Absorption spectrum of Rhodamine 110

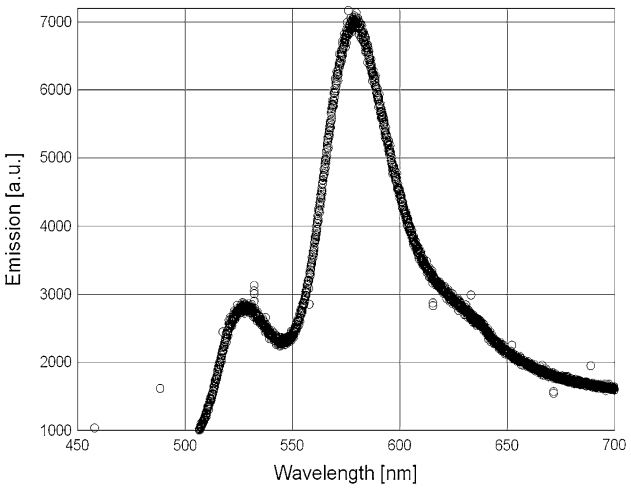

Fig. 7 Emission spectrum of a mixture of Rhodamine B and Rhodamine 110 excited with a Nd:YAG laser ($\lambda_{ex} = 532$ nm)

in front of the CCD for Rhodamine 110 which only transmits light with a wavelength smaller than 530 nm.

The temperature calibration is performed according to Sakakibara and Adrian (2004). We recorded two sets of reference images at uniform and known temperatures T_1 and T_2 and applied a linear interpolation to calculate the temperature

$$T = \frac{\gamma - \gamma_2}{\gamma_2 - \gamma_1}(T_2 - T_1) + T_2, \quad (5)$$

where γ_1 is the intensity ratio at temperature T_1, respectively γ_2 the intensity ratio at T_2. This calibration is evaluated for each pixel. To account for any backscattering effects of the seeding particles the calibration is performed with the flow being seeded. In post-processing, the temperature information is then averaged over an area of 8×8 pixels^2 and is then mapped onto the velocity field.

To justify the choice of a linear calibration function, the temperature dependance of Rhodamine B needs to be investigated. To address this aspect measurements are performed in a Rayleigh–Bénard convection cell described in detail by Günther (2001). A measure of 150 µg/l Rhodamine B were diluted in the water-filled convection cell and both walls were kept at constant temperatures ranging from 20 to 50°C. To ensure a homogeneous temperature distribution the fluid was mixed with a magnetic stirrer between the measurements. A Nd:YAG laser was used as exciting light source. Figure 8 depicts the relation between the temperature and the emitted light intensity of Rhodamine B. These results exhibit a linear dependency of the emitted light intensity on the fluid temperature.

Uncertainties in the PLIF measurements originate from the calibration and the measurement itself. During the calibration process the fluid temperature of the measurement plane inside the test section of the channel was recorded with a thermocouple having a sensitivity of 0.1°C. For each temperature, the calibration is performed with an image averaged over 10 recordings. The concentration of the tracer dyes and the optical path is kept constant between calibration and measurement, thus these effects are considered in the calibration function. We estimate the uncertainty in our temperature measurements to be in the order of 1°C, which corresponds to approximately 4% of the bulk temperature ($T_B = 23$°C), or 18% when scaled with the difference of 5.5°C between the wavy wall temperature and the bulk fluid temperature.

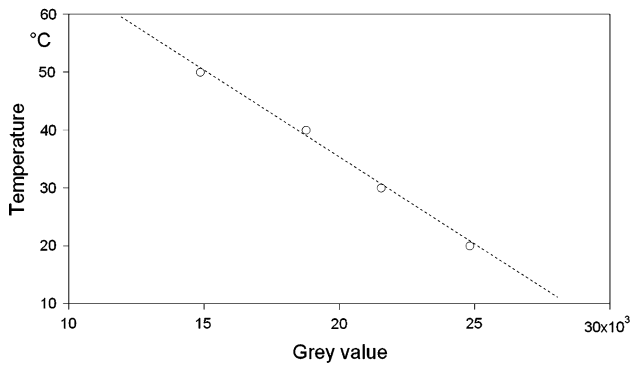

Fig. 8 Relation between the temperature and the emitted light intensity of Rhodamine B

4 Results

The field of view (FOV) of the measurements in the (x,y)-plane covers the whole region between the wavy surface and the flat top wall (FOV 1.45 H (streamwise) $\times$ 1.12 H (vertical)). The spatial resolution of the PIV data in this plane of measurement is 0.016 H, which corresponds to 480 µm. The spatial resolution of the PLIF data is 0.009H, respectively 274 µm.

The field of view for the measurements in the (x,z)-plane is 0.87 H (streamwise) $\times$ 1.14 H (spanwise), which corresponds to a spatial resolution of the PIV data of 0.013 H, respectively 384 µm. The spatial resolution of the PLIF data in this plane of measurement is 0.0067H, or 200 µm. The laser light sheet is adjusted to a plane at $y/H = 0.07$ above the wavy surface.

To characterize the influence of the heated bottom surface on the velocity field, we plot profiles of turbulence quantities at constant streamwise positions along one wavelength, where $x/H = 0.00$ and $x/H = 1.00$ denotes the wave crest, $x/H = 0.50$ the wave trough.

4.1 Mean velocity profiles

Figure 9 depicts the profiles of the normalized mean velocity $\langle u \rangle / U_B$ for a Reynolds number of $Re_H = 1{,}025$ (unheated) and $Re_H = 1{,}100$ (heated). In the unheated case, an asymmetric mean velocity profile is observed. The location of maximum flow velocity is shifted towards the flat top wall and is found at a vertical coordinate of $y/H = 0.65$. This is consistent with earlier studies of isothermal flows over wavy walls at higher Reynolds numbers (e.g. Kruse et al. 2006). In the heated case also an asymmetric velocity profile is observed, however the location of maximum flow velocity is shifted towards the heated bottom surface ($y/H = 0.4$). In the flow region near the heated surface ($y/H < 0.2$) a higher mean streamwise velocity compared to the unheated case is observed. Negative values of the mean velocity in the region of the wave trough ($x/H = 0.50$) in the heated case indicate a separated flow region, which is not observed in the isothermal case.

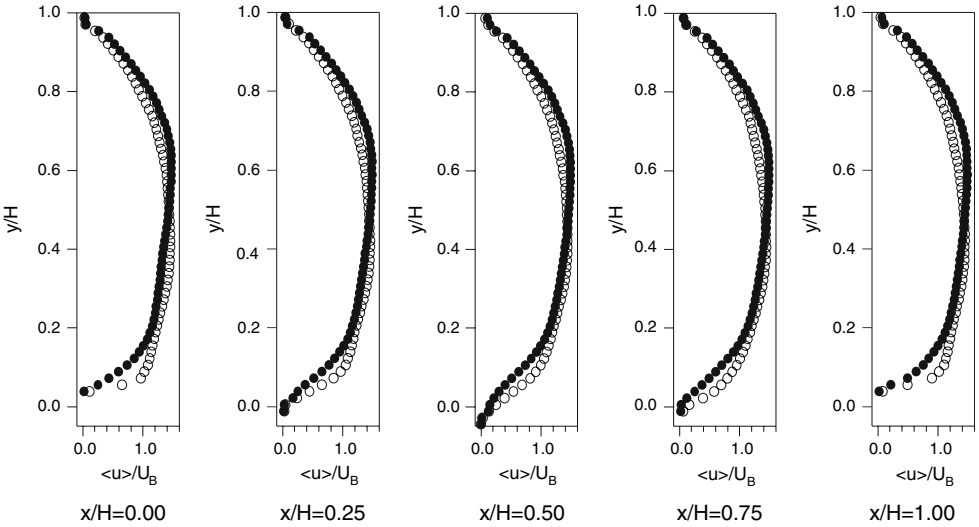

Fig. 9 Profiles of the mean velocity $\langle u \rangle / U_B$ along one wavelength for Reynolds numbers of $Re_H = 1{,}025$ (unheated, *filled circle*) and $Re_H = 1{,}100$ (heated, *circle*). The locations $x/H = 0.00$ and $x/H = 1.00$ correspond to the wave crest, $x/H = 0.50$ to the wave trough

4.2 Root mean square of velocity fluctuations

To further characterize the influence of the heated wavy surface, we calculate the normalized root mean squares of the streamwise velocity fluctuations $\sqrt{\langle u'^2 \rangle}/U_B$, respectively $\sqrt{\langle v'^2 \rangle}/U_B$ in vertical direction. Figure 10 depicts the profiles of the root mean square of the streamwise velocity fluctuation along one wavelength for the Reynolds number $Re_H = 1{,}025$ (unheated) and $Re_H = 1{,}100$ (heated). For the heated case, in general, larger values of the root mean square are found, especially in the region near the heated wavy surface. At the location of the wave crest, i.e. $x/H = 0.00$ and $x/H = 1.00$, the profiles nearly overlap. Downstream and upstream of the wave crest and in the wave trough a maximum is found at a vertical position of approximately $y/H = 0.1$. This indicates that the fluid inside the wave trough accumulates more heat resulting in higher local fluid velocities compared to the isothermal case. A second maximum of the root mean square of the streamwise velocity fluctuations is located in the upper half of the channel near the flat top wall at $y/H \approx 0.8$. This could be an indication of large-scale thermal structures reported in an earlier study (Kruse and Rudolf von Rohr 2006), which are identified by a proper orthogonal decomposition as streamwise-oriented, coherent flow structures. Figure 11 depicts the profiles of the root mean square of the vertical velocity fluctuations along one wavelength for the Reynolds number $Re_H = 1{,}025$ (unheated) and $Re_H = 1{,}100$ (heated). In the profiles, the influence of buoyancy due to the resulting fluid motion in vertical direction is observed. In the region between the heated bottom surface and the dimensionless coordinate of $y/H = 0.8$ larger rms values of the vertical velocity fluctuations are found. These results allow to determine the region of the flow which is directly affected by mixed convection.

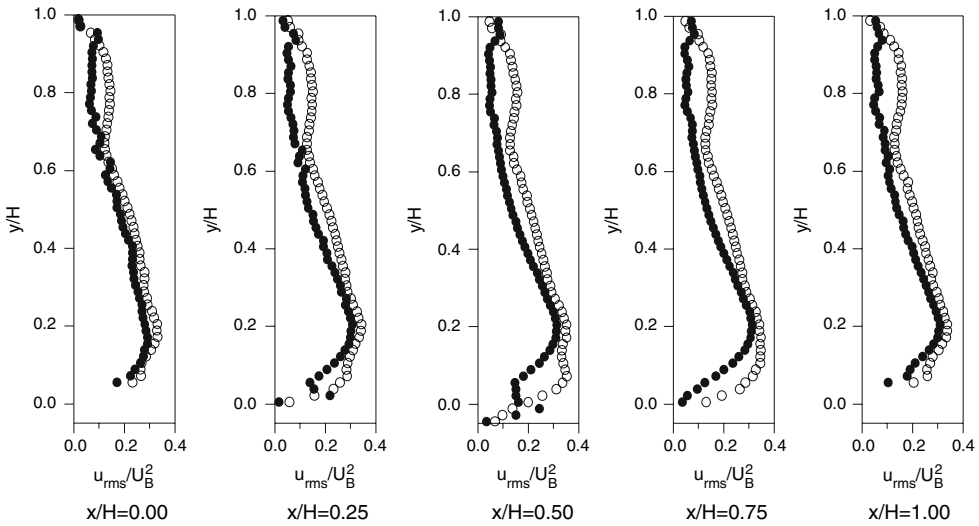

Fig. 10 Profiles of the root mean square of the streamwise velocity fluctuation $\sqrt{\langle u'^2 \rangle}/U_B$ along one wavelength for Reynolds numbers of $Re_H = 1{,}025$ (unheated, *filled circle*) and $Re_H = 1{,}100$ (heated, *filled circle*). The locations $x/H = 0.00$ and $x/H = 1.00$ correspond to the wave crest, $x/H = 0.50$ to the wave trough

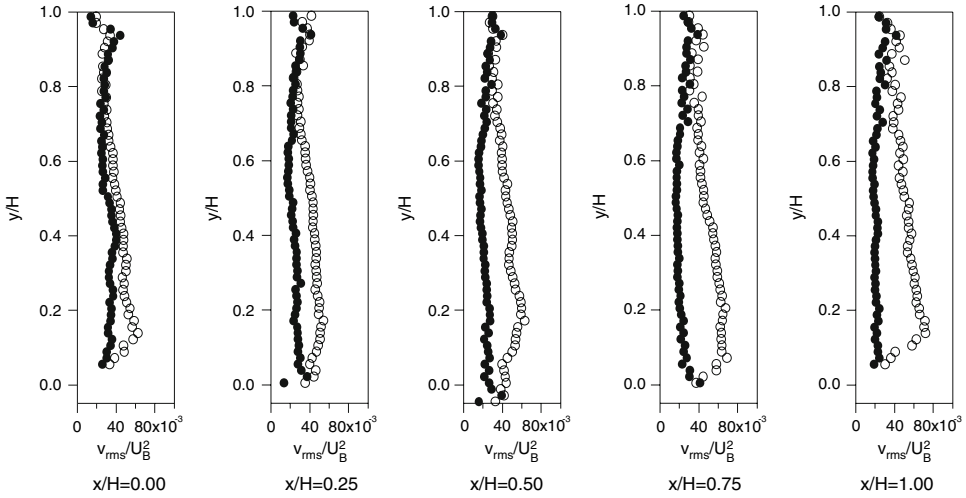

Fig. 11 Profiles of the root mean square of the vertical velocity fluctuation $\sqrt{\langle v'^2 \rangle}/U_B$ along one wavelength for Reynolds numbers of $Re_H = 1{,}025$ (unheated, *filled circle*) and $Re_H = 1{,}100$ (heated, *circle*). The locations $x/H = 0.00$ and $x/H = 1.00$ correspond to the wave crest, $x/H = 0.50$ to the wave trough

4.3 Reynolds stress

The flow over waves is associated with a shear layer developing after the wave crest and extending over the whole wavelength. For mixed convection this shear layer is expected to be intensified through the interaction between the mean flow and the upward fluid motion due to buoyancy. Figure 12 depicts the profiles of the Reynolds stress along one wavelength for the Reynolds number $Re_H = 1{,}025$ (unheated) and $Re_H = 1{,}100$ (heated). Larger values of the Reynolds stress are found in the region between the heated wavy surface and the location $y/H = 0.6$. The location of the maximum changes from a vertical coordinate of $y/H = 0.15$ for the wave crests to $y/H = 0.10$ in the wave trough. At the upstream side of the wave crest ($x/H = 0.75$) a pronounced Reynolds stress profile is found. This indicates that the mixed convection is also influenced by the local curvature of the wall.

4.4 Mean temperature field and scalar fluxes

Figure 13 depicts the contour of the mean temperature $\langle T \rangle$ normalized with the bulk temperature T_B. The heat transfer from the heated wavy surface to the fluid is observed by the layer of fluid along the surface with elevated temperature. The thickness of the layer increases at the upstream side of the wave, which is consistent with the observations for the velocity field and the turbulence statistics. No temperature changes are observed in the mean temperature field for a region $y/H > 0.2$. To address the transport of temperature we calculate the normalized heat fluxes $\langle u'T' \rangle/(U_B T_B)$, respectively $\langle v'T' \rangle/(U_B T_B)$, from the simultaneous measurements. Figure 14 depicts the contours of the turbulent heat flux components in the (x,y)-plane. For the vertical component (Fig. 14b) the largest values are observed along the heated wavy surface, which causes the transport of heat from the wall to the bulk of the fluid. This region of

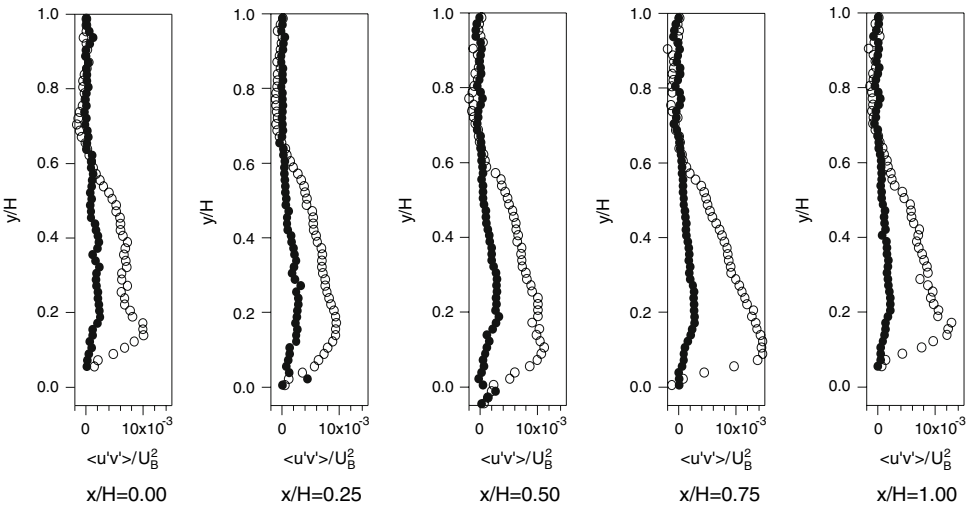

Fig. 12 Profiles of the Reynolds stress $\langle u'v' \rangle/U_B^2$ along one wavelength for Reynolds numbers of $Re_H = 1{,}025$ (unheated, *filled circle*) and $Re_H = 1{,}100$ (heated, *circle*). The locations $x/H = 0.00$ and $x/H = 1.00$ correspond to the wave crest, $x/H = 0.50$ to the wave trough

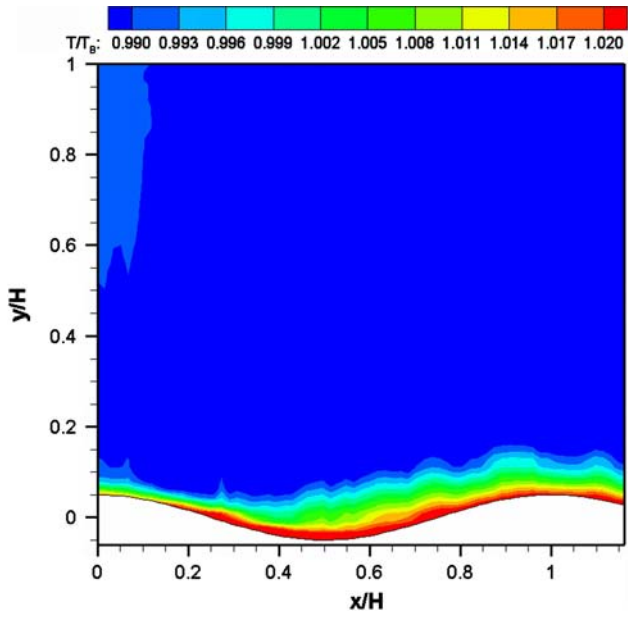

Fig. 13 Contour of the mean temperature profile $\langle T \rangle / T_B$ in the (x,y)-plane at $Re_H = 1{,}100$

increased vertical heat flux is not found to be parallel to the wavy wall, but increases in the region of the wave trough. This location corresponds to the developing shear layer which is formed after the wave crest and extends over the wave trough. The maximum of the streamwise heat flux (Fig. 14a) is found in a region above the wavy wall ($0.05 < y/H < 0.20$), with a local maximum at the upstream side of the wave. By comparing the heat flux components with the profiles of the Reynolds shear stress (Fig. 12), a correlation between the two quantities is observed. The locations of increased momentum transport coincide with the regions of increased scalar transport. The values found for the streamwise component of the heat flux are in the order of a magnitude larger compared to the vertical component.

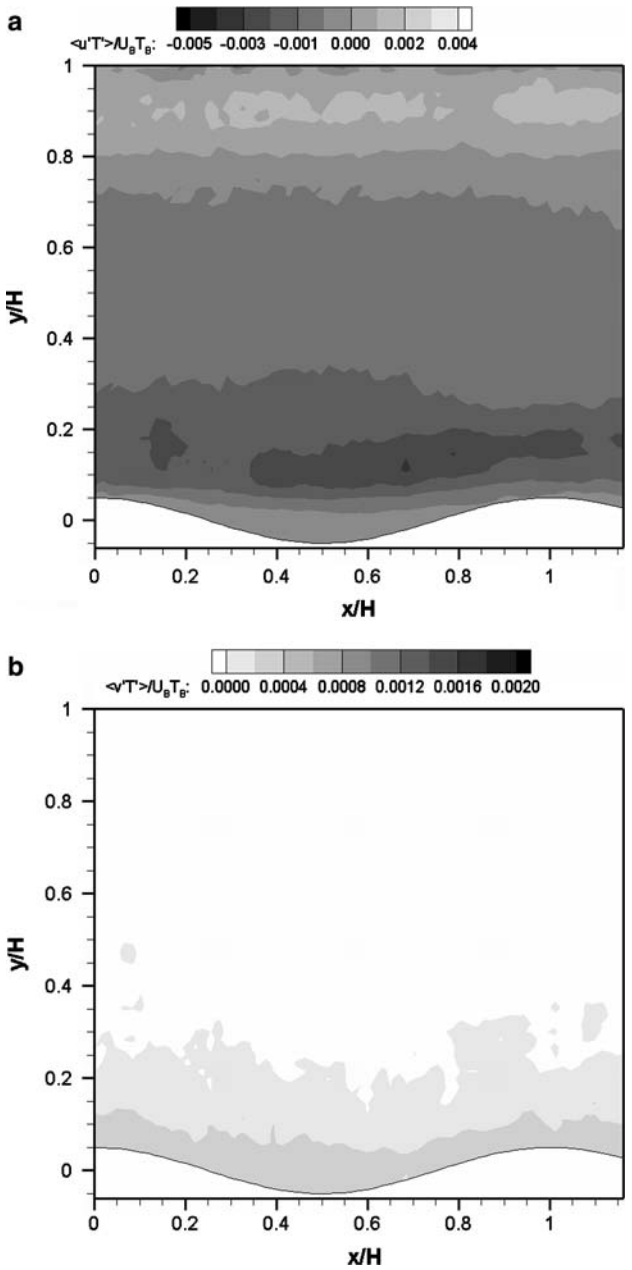

Fig. 14 Contour plot of the turbulent heat flux components in the (x,y)-plane

4.5 Proper orthogonal decomposition of the velocity field

To extract the most dominant flow structures we perform a proper orthogonal decomposition (POD) or Karhunen-Loève (KL) decomposition of the velocity field by using the method of snapshots (Sirovich 1987; Berkooz et al. 1993; Liu et al. 2001). In the following, this method is reviewed briefly. We consider a scalar quantity $\xi(\mathbf{x},t)$, which may represent a velocity component, $u_i(\mathbf{x},t)$, a temperature, $T(\mathbf{x},t)$, or a concentration of a species, $c(\mathbf{x},t)$, at discrete times t_i with $i = 1,\ldots, M$, and $1,\ldots, N$ discrete locations within a two-dimensional plane. Thus, a spatiotemporal set of data can be written as the following $N \times M$ matrix:

$$\mathbf{X} = \{\mathbf{X}_i\}_{i=1}^{M} = \begin{bmatrix} \xi_{11}, \xi_{12}, \ldots, \xi_{1M} \\ \xi_{21}, \xi_{22}, \ldots, \xi_{2M} \\ \vdots \\ \xi_{N1}, \xi_{N2}, \ldots, \xi_{NM} \end{bmatrix} \tag{6}$$

with $\mathbf{X}_i = [\xi_1, \xi_2, \ldots, \xi_N]^{\mathrm{T}}$. The mean is computed by

$$\overline{\mathbf{X}} = \frac{1}{M} \sum_{i=1}^{M} \mathbf{X}_i. \tag{7}$$

For the fluctuations, it then follows that

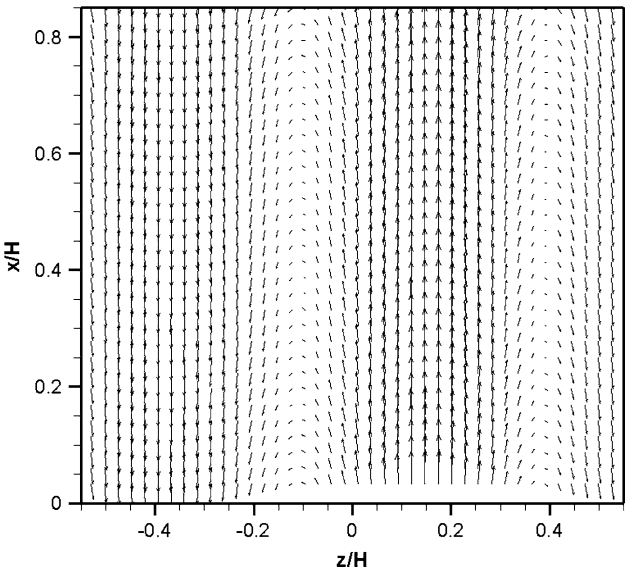

Fig. 15 Vector field of the first POD mode for a decomposition of $\mathbf{u}/U_B(x,y/H = 0.10,z,t)$ with an energy contribution of 27.4% in the (x,z)-plane (ensemble size 1,000 images)

$$\mathbf{X}'_i = \mathbf{X}_i - \overline{\mathbf{X}}, \quad i = 1,\ldots,M. \tag{8}$$

Applying the method of snapshots, a $M \times M$ covariance matrix $\mathbf{C}$ can be computed, which reads

$$\mathbf{C}_{ij} = \left\langle \mathbf{X}'_i \mathbf{X}'_j \right\rangle, \quad i,j = 1,\ldots,M, \tag{9}$$

where $\langle \cdot,\cdot \rangle$ is the Euclidean inner product. Since the covariance matrix is symmetric, its eigenvalues, λ_i, are non-negative, and its eigenvectors, $\phi_i, i = 1,\ldots, M$, form a complete orthogonal set. The orthogonal eigenfunctions are thus defined as:

$$\Pi^{[k]} = \sum_{i=1}^{M} \phi_i^{[k]} \mathbf{X}'_i, \qquad k = 1,\ldots,M, \tag{10}$$

where $\phi_i^{[k]}$ is the ith component of the kth eigenvector. The total energy E is obtained through summation of the eigenvalues:

$$E = \sum_{i=1}^{M} \lambda_i.$$

The fractional contribution of each eigenfunction to the total energy is given by the fractional contribution of its associated eigenvalue:

$$\frac{E_k}{E} = \frac{\lambda_k}{E}. \tag{11}$$

For a more detailed description of the implementation of this technique to two-dimensional PIV data, we refer to Kuhn et al. (2007).

Figure 15 depicts the vector field of the first POD mode for a decomposition of $\mathbf{u}/U_B(x,y/H = 0.10,z,t)$, where $\mathbf{u}$ denotes the measured velocity vector $(u,w)^{\mathrm{T}}$. The contribution of the first POD mode to the total energy of the mixed convective flow is 27.4% which expresses its dominance. Figure 16 depicts the fractional and cumulative kinetic energy contribution of the first 15 POD modes. It is observed that the first 5 modes capture nearly 80% of the kinetic energy of the flow. Thus the dominant flow features can be described by addressing only the first few POD modes. The vector field visualizes the structure of the dominant eigenmode as streamwise-oriented, counter-rotating vortices. The spanwise scale , defined as the distance between the cores of the longitudinal flow structures characterized by the same direction of velocity fluctuations, is identified as $1.1H$. This value is smaller than for the first POD mode for the isothermal turbulent flow over waves (Kruse et al. 2006). Thus, we identify an influence of mixed convection on longitudinal flow structures present in the flow field.

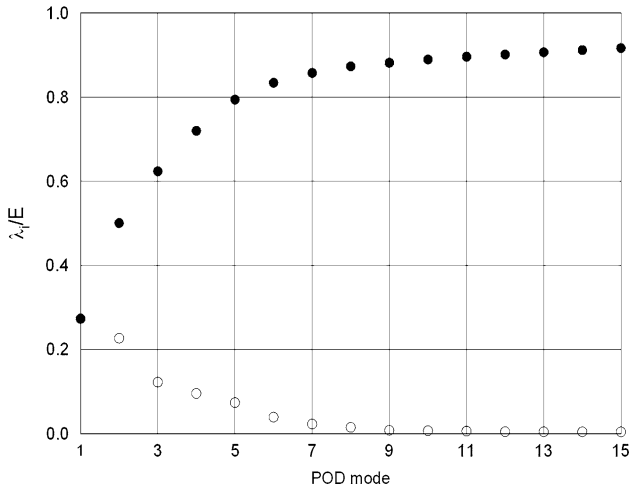

Fig. 16 Fractional (*circle*) and cumulative (*filled circle*) kinetic energy contribution from eigenvalues for a decomposition of $\mathbf{u}/U_B(x,y/H = 0.10,z,t)$ (ensemble size 1,000 images)

4.6 Scalar fluxes

Figure 17 depicts the vector plot of the heat flux in the (x,z)-plane. By comparing this figure with the vector plot of the first POD mode an agreement of the spanwise scales is found. The maximum of scalar transport occurs in the region between the cores of the longitudinal flow structures, i.e. the region of maximum rotation ($-0.2 < z/H < 0.0$ and $0.3 < z/H < 0.5$). Thus, the measurements in the (x,z)-plane verify the observations in the (x,y)-plane, locations of increased momentum transport coincide with regions of increased scalar transport. In addition, the scalar transport is increased at the upstream side of the wave ($x/H > 0.50$), indicated by the broadening of the heat flux vector field.

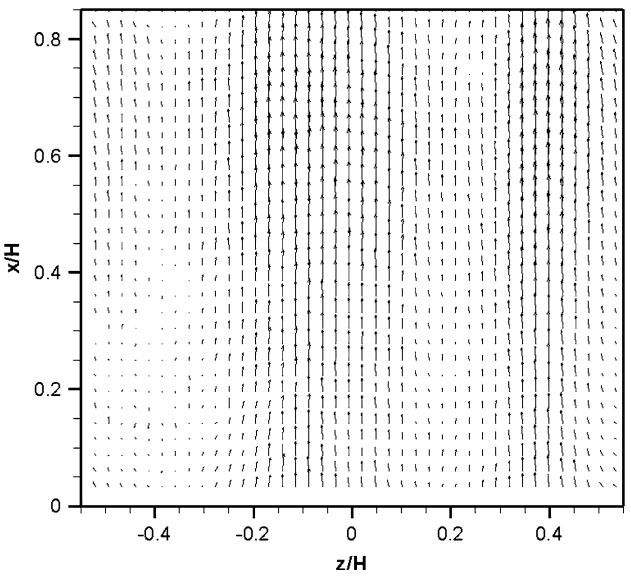

Fig. 17 Vector plot of the turbulent heat flux in the (x,z)-plane

Thus, we also identify an influence of the bounding surface geometry on scalar transport processes.

5 Conclusions

We apply a combined DPIV/PLIF technique to simultaneously measure the velocity and temperature fields of a mixed convective flow over a wavy surface. Therefore, we employed two-color PLIF with the fluorescent dye combination Rhodamine B/Rhodamine 110 excited with a Nd:YAG laser. The flow between the flat top and heated wavy bottom surface is investigated at the Reynolds numbers $Re_H = 1{,}100$ (heated), respectively $Re_H = 1{,}025$ (unheated). By recording long image series the statistics of the velocity and temperature fields are calculated and we discuss the influence of mixed convection on turbulence quantities and scalar transport properties.

We identified a shift of the mean velocity profile in the vicinity of the heated surface and a separation zone downstream of the wave, both effects not present in the isothermal case. By calculating the root mean square values of the velocity fluctuations and the Reynolds stress we concluded that momentum transport is increased for the mixed convection regime. The maximum of the heat flux components measured in the (x,y)-plane coincides with the maximum of the Reynolds shear stress. Thus, we conclude that locations of increased momentum transport coincide with the regions of increased scalar transport. These observations are verified by the measurements in the (x,z)-plane. There we apply a proper orthogonal decomposition to extract the most dominant flow structures which appear as streamwise-oriented, counter-rotating vortices. Their spanwise scale agrees with the scale of the heat flux vector field in this plane of measurement. The maximum of the heat flux is located between the cores of the extracted longitudinal flow structures. In addition, we find an influence of the bounding surface on the transport processes, visualized by the shape of the mean temperature profile and the increasing heat flux at the upstream region of the wave.

By applying a combination of DPIV and two-color PLIF to simultaneously measure the velocity and temperature fields, we show a correlation of momentum and scalar transport in mixed convective flow over waves.

Acknowledgments We gratefully acknowledge financial support from the Swiss National Science Foundation (SNF). Measurement technology is partially provided by ILA GmbH.

References

Adrian RJ (1991) Particle-imaging techniques for experimental fluid mechanics. Annu Rev Fluid Mech 23:261–304

Berkooz G, Holmes P, Lumley JL (1993) The proper orthogonal decomposition in the analysis of turbulent flows. Annu Rev Fluid Mech 25:539–575

Brooke JW, Hanratty TJ (1993) Origin of turbulence-producing eddies in a channel flow. Phys Fluids A5(4):1011–1022

Bruchhausen M, Guillard F, Lemoine F (2005) Instantaneous measurement of two-dimensional temperature distributions by means of two-color planar laser induced fluorescence (PLIF). Exp Fluids 38:123–131

Cherukat P, Na Y, Hanratty TJ, McLaughlin JB (1998) Direct numerical simulation of a fully developed turbulent flow over a wavy wall. Theor Comp Fluid Dyn 11:109–134

Coolen MCJ, Kieft RN, Rindt CCM, van Steenhoven AA (1999) Application of 2D-LIF temperature measurements in water using a Nd:YAG laser. Exp Fluids 27:420–426

Dabiri D, Gharib M (1991) Digital particle image thermometry: the method and implementation. Exp Fluids 11:77–86

Dellil AZ, Azzi A, Jubran BA (2004) Turbulent flow and convective heat transfer in a wavy wall channel. Heat Mass Transfer 40:793–799

Günther A (2001) Large-scale structures in Rayleigh–Bénard convection and flow over waves. PhD thesis, ETH Zürich, Switzerland

Günther A, Rudolf von Rohr P (2003) Large-scale structures in a developed flow over a wavy wall. J Fluid Mech 478:257–285

Henn DS, Sykes RI (1999) Large-eddy simulation of flow over wavy surfaces. J Fluid Mech 383:75–112

Incropera FP, DeWitt DP (2002) Fundamentals of heat and mass transfer. Wiley, London

Karasso PS, Mungal MG (1997) PLIF measurements in aqueous flows using the Nd:YAG laser. Exp Fluids 23:382–387

Kruse N (2005) Isothermal and non-isothermal turbulent flow over solid waves. PhD thesis, ETH Zurich, Switzerland, http://e-collection.ethbib.ethz.ch/show?type=diss&nr= 16031

Kruse N, Rudolf von Rohr P (2006) Structure of turbulent heat flux in a flow over a heated wavy wall. Int J Heat Mass Transfer 49(19–20):3514–3529

Kruse N, Günther A, Rudolf von Rohr P (2003) Dynamics of large-scale structures in turbulent flow over a wavy wall. J Fluid Mech 485:87–96

Kruse N, Kuhn S, Rudolf von Rohr P (2006) Wavy wall effects on turbulence production and large-scale modes. J Turbulence 7(31):1–24

Kuhn S, Wagner C, Rudolf von Rohr P (2007) Influence of wavy surfaces on coherent structures in a turbulent flow. Exp Fluids 43:251–259

Liu Z, Adrian RJ, Hanratty TJ (2001) Large-scale modes of turbulent channel flow: transport and structure. J Fluid Mech 448:53–80

Maughan JR, Incropera FP (1989) Regions of heat transfer enhancement for laminar mixed convection in a parallel plate channel. Int J Heat Mass Transfer 33:555–570

Metwally HM, Manglik RM (2004) Enhanced heat transfer due to curvature-induced lateral vortices in laminar flows in sinusoidal corrugated-plate channels. Int J Heat Mass Transfer 47:2283–2292

Osborne DG, Incropera FP (1985a) Experimental study of mixed convection heat transfer for transitional and turbulent flow between horizontal, parallel plates. Int J Heat Mass Transfer 28(7):1337–1344

Osborne DG, Incropera FP (1985b) Laminar, mixed convection heat transfer for flow between horizontal plates with asymmetric heating. Int J Heat Mass Transfer 28:207–217

Raffel M, Willert C, Kompenhans J (1998) Particle Image Velocimetry. A practical guide. Springer, Heidelberg

Rush TA, Newell TA, Jacobi AM (1999) An experimental study of flow and heat transfer in sinusoidal wavy passages. Int J Heat Mass Transfer 42:1541–1553

Sakakibara J, Adrian RJ (1999) Whole field measurements of temperature in water using two-color laser-induced fluorescence. Exp Fluids 26:7–15

Sakakibara J, Adrian RJ (2004) Measurement of temperature field of a Rayleigh–Bénard convection using two-color laser-induced fluorescence. Exp Fluids 37:331–340

Scarano F (2002) Iterative image deformation methods in PIV. Meas Sci Technol 13:R1–R19

Scarano F, Riethmuller ML (2000) Advances in iterative multigrid PIV image processing. Exp Fluids 29:S51–S60

Sirovich L (1987) Turbulence and the dynamics of coherent structures. Part I. Coherent structures. Quart Appl Math XLV:561–571

Wagner C, Kuhn S, Rudolf von Rohr P (2007) Scalar transport from a point source in flows over wavy walls. Exp Fluids 43:261–271

Westerweel J (1997) Fundamentals of digital particle image velocimetry. Meas Sci Technol 8:1379–1392

Yu CH, Chang MY, Huang CC, Lin TF (1997a) Unsteady vortex roll structures in a mixed convective air flow through a horizontal plane channel: a numerical study. Int J Heat Mass Transfer 40(3):505–518

Yu CH, Chang MY, Lin TF (1997b) Structures of moving transverse and mixed rolls in mixed convection of air in a horizontal plane channel. Int J Heat Mass Transfer 40(2):333–346